Acta Materialia 190 (2020) 93–104

Contents lists available at ScienceDirect

Acta Materialia

journal homepage: www.elsevier.com/locate/actamat

Full length article

# Tantalum and zirconium induced structural transitions at complex [111] tilt grain boundaries in copper

T. Meiners[a], J.M. Duarte[a], G. Richter[b], G. Dehm[a], C.H. Liebscher*[,a]

[a] Max-Planck-Institute for Iron Research GmbH Germany
[b] Max-Planck-Institute for Intelligent Systems Germany

ARTICLE INFO

*Article History:*
Received 4 October 2019
Revised 27 February 2020
Accepted 28 February 2020
Available online 18 March 2020

*Keywords:*
grain boundaries
atomic structure
transmission electron microscopy
structural transitions
grain boundary pinning

ABSTRACT

Alloying nanocrystalline copper (Cu) with immiscible elements, such as tantalum (Ta) and zirconium (Zr), is a promising technique to manipulate grain boundary properties and by this suppress grain growth at elevated temperatures. However, insights on the atomistic origins on the influence of impurity elements on grain boundaries are lacking. In this study, the atomistic effects of Ta and Zr on [111] tilt grain boundaries in Cu are investigated by high resolution scanning transmission electron microscopy techniques. In case of Ta, the formation of spherical, nano-scale precipitates in close vicinity to the grain boundaries is observed, but no sign of segregation. The particles induce a repelling force to migrating boundaries and act as local pinning points. The segregation of Zr is observed to occur either at confined grain boundary steps or homogeneously along the boundaries without steps. In both cases a strong disordering of the defect or grain boundary structure is revealed. Furthermore, at low Zr concentrations it induces structural grain boundary transitions and partial atomic reordering of the grain boundary structural units.



## 1. Introduction

Grain boundaries (GBs) have been investigated over many decades because of their enormous importance to tailor material properties [1–5]. Even though many experimental and theoretical studies have been employed to unravel the structure, energy, mobility and diffusion behavior of special GBs, a detailed understanding of the atomistic mechanisms of GB segregation effects and their impact on GB properties is lacking [1,4,6–11]. The main challenge to establish a generalized picture in this field results from the huge variety of GB types [2], the difficulty to experimentally access their atomic structure and to correlate it directly to the GB properties. Mostly atomistic simulations are employed to explore GB structures and effects of impurity segregation, although these studies are limited by the accessibility of reliable semi-empirical atomic potentials [1,12–15].

Already ~50 years ago the structural unit (SU) model was introduced in order to describe the atomic structure of special coincident site lattice (CSL) GBs by repeating 2D building blocks [1,12,16]. A GB that consists of only one single unit type is called a delimiting boundary. The SU model predicts that each GB with misorientation $\Theta$ can be constructed using only the units from the delimiting GBs. Many theoretical studies focused on the description of the structural units of different symmetric and asymmetric GBs [1,6,7,12]. Frost et al. [6] presented a catalogue of predicted structures for [001], [011] and [111] symmetric tilt GBs in face-centered cubic (fcc) hard sphere crystals. Wang et al. [7] followed the approach and presented structures of [001] and [111] tilt GBs and their energies. However, more recent studies have shown that the SU model does not work in general for all kinds of GB, e.g in low stacking fault materials and for longperiod GBs [17,18]. Therefore, the SU model was revisited and extended by Han et al. [19] including stable and metastable GB structures as delimiting boundaries.

The development of aberration-corrected transmission electron microscopes (TEM) made it possible to experimentally access the atomic structure and chemistry of GBs. In recent years, several studies explored the atomic arrangements of special tilt GBs in ceramic, metallic and semiconductor systems [9,20–25]. Yu et al. also showed that periodic segregation pattern can be formed at more general GBs and that these reconstructions are not dependent on the grain misorientation but rather on the orientation of the terminating grain surfaces [25]. In combination with complementing atomistic simulations it is possible to unravel intrinsic GB properties, such as segregation behavior or cohesive properties. These detailed insights enabled GB engineering as a major research field in order to tailor materials properties by manipulating the structure and chemistry of GBs [26]. Introducing impurity elements at GBs is a promising way to modify specific GB properties, such as cohesion, mobility and energy. The reason for such property deviations can be explained by structural and chemical transitions, which are difficult to access at atomic

* Corresponding author.
*E-mail address:* liebscher@mpie.de (C.H. Liebscher).

https://doi.org/10.1016/j.actamat.2020.02.064

resolution due to experimental restrictions [10,27–29]. Recently, Peter et al. reported a segregation-induced nano-faceting transition of an asymmetric copper (Cu) tilt GB [24]. Only the combination of atomic resolution scanning TEM (STEM) and molecular dynamics simulations was able to reveal the underlying atomistic and thermodynamic origins for the nanofacet formation.

An emerging field where GBs and their transitions play an important role are nanocrystalline (nc) and nano-structured materials [30–35]. They have recently received broad attention because of their unique properties. Especially the mechanical behavior of such materials is to mention here since the yield and flow stress as well as the hardness can increase quite significantly [36–39]. Nanocrystalline Cu is a particularly interesting candidate because of the excellent electrical and thermal conductivity of Cu [5] and its remarkably high strength [36,40]. However, rapid grain growth and the resulting instability of the microstructure at elevated temperatures strongly limit its commercial application. A way to stabilize the grain structure up to the melting point has been achieved by alloying with immiscible elements. It has been proposed that these elements tend to segregate to GBs and either kinetically or thermodynamically prevent grain growth. The kinetic approach utilizes second phase precipitation to pin migrating GBs, a process know as Zener pinning [41,42]. In the thermodynamic approach, the GB free energy is reduced by solute segregation and thus the driving force for grain growth is decreased [43–45]. Two prominent candidates for stabilizing the nc grain structure are zirconium (Zr) and tantalum (Ta).

The formation of nano-scale Ta clusters or precipitates in nc Cu have been shown to increase the strength and stability of the microstructure, referred to as kinetic approach. In ref. [46], the hardness was found to increase by more than a factor of 2 compared to pure Cu with comparable grain size. Close to the melting temperature the alloy suffered less from grain growth and could retain the extreme hardness. At the same time, the Cu matrix maintains its excellent electrical and thermal properties [47,48]. However, a major disadvantage is the production of these alloys. Not only the solubility of Ta in Cu is neglegible [49], but also the diffusion of Ta inside the Cu matrix is close to zero at temperatures below 1000°C [46]. Furthermore, the underlying atomistic mechanisms of Ta segregation to GBs and GB pinning have been explored mainly by simulations. Only a few detailed TEM studies exist, investigating the effect of Ta on the atomistic mechanisms of GBs, e.g ref. [46,50].

Zirconium was seen as an excellent candidate to stabilize nc Cu due to its poor solubility in Cu (0.12 at % at 972 °C [51]), the tendency to segregate to GBs and glass phase formation [52]. Atwater et al. [53] showed that adding only 1 at% Zr can stabilize the nanoscale grain size by forming small scale intermetallic phases and Zirconia ($ZrO_2$) at GBs. In contrast, Khalajhedayati et al. [52] reported the formation of amorphous intergranular films, which are assumed to reduce the GB energy and therefore the driving force for GB migration.

In this study, the effect of Ta and Zr on the atomic structure is investigated. In order to observe the atomic structure of GBs in TEM, both grains need to share a common zone axis parallel to the electron beam direction, which is true for tilt GBs. This can be achieved by growing Cu thin films onto sapphire (0001) substrates by molecular beam epitaxy (MBE), which is explained in detail in Ref. [54]. Thus, defined [111] tilt GBs are produced in order to systematically study the same GB structures and possible structural transitions by the addition of solute atoms (Ta and Zr). The representative GBs in this work are two symmetric $\Sigma 19b$ and corresponding asymmetric variants, with deviations of maximum $\sim 6°$ from the symmetric orientation. The $\Sigma 19b$ is amongst the most common high angle tilt GBs in these films and can be easily reproduced. It was found that they occur in two symmetric and vicinal variants. The GBs exhibit long period structural units, which can be further decomposed into subunits. Even though only the GB inclination changed by 30°, the two GBs show strongly differing atomic structures, which do not agree with the SU model as described above. The Cu films are alloyed by sputter depositing Ta and Zr thin films at room temperature followed by a subsequent post-deposition annealing treatment and it is shown that GB diffusion is fast enough to introduce large amounts of Ta and Zr into the GBs. The effect of both impurity elements on the atomic structure is investigated by aberration-correct STEM. It is shown that this is a simple process to introduce spherical, nano-scale Ta precipitates at GBs, which act as local GB pinning points by bending the local GB plane. The segregation behavior of Zr is observed to occur in two different ways. At a planar asymmetric GB, Zr homogeneously decorates the GB and causes a strong disordering of its atomic structure. Confined Zr segregation to GB steps is observed for a nano-faceted GB, where the steps are more disordered compared to the clean GB steps. At the symmetric GB facets structural transitions compared to the clean GB facets are observed.

## 2. Experimental details

Cu thin films were grown by MBE at room temperature on (0001) oriented sapphire substrates followed by a post-deposition annealing for 4 h at 400 °C. For the segregation experiments, the Cu film surface was sputter cleaned prior to deposition of Ta and Zr thin films. Subsequently, 50 nm Ta and 100 nm Zr films were deposited each separately at room temperature on a small piece of the Cu film. The Zr/Cu film was annealed for 5 h at ∼ 400°C under high vacuum conditions. The annealing temperature and time were chosen rather small in order to prevent the formation of intermetallic phases at the GB and the sample surface. The Ta/Cu film, however, was annealed for 24 h at ∼ 600°C. Since Ta diffusion in Cu is almost zero, a much higher temperature and longer annealing time was chosen in order to activate GB diffusion. A higher temperature for higher diffusion was not chosen to be sure that the films remain thermally stable and prevent dewetting of the Cu film. Therefore, the temperature was selected to be at least half of the absolute melting temperature of Cu. Thin film texture and global grain structure was determined by electron backscatter diffraction (EBSD) in a JSM-6490 (JEOL) operated at an acceleration voltage of 30 kV. TEM specimens of special GBs were prepared either by a site-specific plan-view focused ion beam (FIB) lift-out as described in ref. [55,56] or as conventional cross-section lift-outs using a dual beam SEM / FIB instrument Helios Nanolab 600i (Thermo Fischer Scientific). EBSD has been performed only on the pure Cu films, since no diffraction pattern could be recorded through the remaining Ta and Zr. STEM imaging was performed in a probe-corrected FEI Titan Themis 60–300 (Thermo Fischer Scientific) S/TEM equipped with a high-brightness field emission gun and gun monochromator operated at an accelaration voltage of 300 keV using a high angle annular dark field (HAADF) detector (Model 3000, Fischione Instruments). The semi-convergence angle was set to 17 mrad and HAADF images were recorded with a collection angle range of 73–200 mrad and a probe current of ∼ 80 pA. For energy-dispersive X-ray spectroscopy (EDS) the probe current was raised to ∼ 150 pA and X-rays were collected with the ChemiSTEM system (Thermo Fisher Scientific). Bright field (BF), dark field (DF) and high resolution TEM imaging was done in an image-corrected FEI Titan Themis 80–300 (Thermo Fischer Scientific) TEM under negative $C_s$ (−10 μm) conditions using an accelerating voltage of 300 keV [57]. APT specimens were prepared by site-specific FIB lift-out using a dual beam workstation Helios Nanolab 600i from Thermo Fischer Scientific. Final low energy cleaning at 5 kV and 40 pA was performed to minimize the Ga content in the sample, which was found to be at the background level in the regions of interest. The measurements were conducted in a LEAP 5000 XR local electrode APT from Cameca Instruments in laser pulsing mode. The specimen temperature was set to 50 *K*, while the laser pulse energy of 85 *pJ* at a frequency of 125 kHz were used to evaporate the sample at a detection rate of 0.7 %. The presence of oxides and other impurity elements was detected only

close to the top surface indicating possible contamination during sample preparation and transfer between instruments. These initial sections, corresponding also to the Zr film, were discarded to focus on the Cu grains and their GBs and no further oxides were found.

## 3. Results

### 3.1. Global thin film grain boundary structure

EBSD reveals that the Cu films grow with [111] texture, as shown by the inverse pole figure (IPF) map in Fig. 1. The film's grain structure is shown in the image quality map (IQM). The grain size can be determined to $\sim 100\ \mu\text{m} \pm 50\ \mu\text{m}$. The large error in average grain size results from a strong scatter in the grain size distribution, which includes grains with diameters of $\sim 300\ \mu$m down to $\sim 10\ \mu$m. The grain size distribution is shown in Fig. 1 (c). Most grains exhibit a round shape (in 3D it is therefore cylindrical due to small film thickness compared to the grain size), which translates to continuous changes in GB inclination along each grain boundary. Approximately 80% of the GBs are low angle and twin boundaries ($\Sigma 3$). The remaining ones are different low $\Sigma$ boundaries, such as $\Sigma 7$ ($\sim 1\%$), $\Sigma 9$ ($\sim 0.3\%$), $\Sigma 19b$ ($\sim 7\%$), $\Sigma 31a$ ($\sim 2.5\%$), $\Sigma 37c$ ($\sim 8\%$). The most frequent GBs are highlighted by colored lines in Fig. 1. The white/black regions in the center of the IPF/IQM illustrates positions from where TEM specimens were extracted by FIB. This procedure ensures that each TEM specimen only contains specific, pre-selected types of CSL boundaries; in the present case a $\Sigma 19b$ GB.

### 3.2. Atomic structure of pure $\Sigma$ 19b grain boundaries

The atomic structure of four different GBs is depicted in Figs. 2 and 3. Two are symmetric $\Sigma 19b$ with a misorientation of $\sim 47^\circ$ and GB habit planes $(25\bar{3})$ and $(18\bar{7})$, which corresponds to a change in boundary plane inclination of $30^\circ$ (see Fig. 2 (a) and (c)). The other two GBs are asymmetric variants of the two symmetric GBs with different GB plane orientation resulting in small angular deviation between $\sim 2$ and $6^\circ$ (Fig. 3 (a) and (d)).

The $\Sigma 19\ b\ (25\bar{3})$ in Fig. 2 (a) is a straight and flat GB, which remains in the symmetric orientation for $\sim 100\,nm$. It is difficult to observe longer segments of these GB orientations, since the grains have mostly a cylindrical shape and therefore the GBs are often stepped or faceted. In between these segments, the same symmetric structural units can be consistently observed. The common description of CSL GB structures is obtained by characteristic structural units (SU) [16,19]. The full SU of the $\Sigma 19\ b\ (25\bar{3})$ can be divided into two sub-units as highlighted by red and green circles in the magnified view of the yellow rectangle of Fig. 2 (b). The filled red circle marks the CSL positions at this GB. The red sub-unit exhibits a square shape formed by 8 atomic columns followed by the green sub-unit, a trapezoid consisting of 4 columns. According to the nomenclature of the SU model, the GB structure can be written as $|ST\cdot ST|$, where $S$ represents the red, squared and $T$ the green, trapezoidal sub-unit. According to [19], the vertical lines | represent one GB period along the GB plane and $''\cdot''$ means that the sub-units are shifted along the GB by a half period. In the entire GB segment these two sub-units alternate and form the GB and disruptions of this sequence at the symmetric segments were not observed. With respect to its appearance, this GB structure is termed zipper structure in the following.

The $\Sigma\ 19\ b\ \left(18\bar{7}\right)$ shows a very different atomic structure (see Fig. 2 (c)) with a change in GB inclination by $30^\circ$. This boundary also remains straight over a length of $\sim 100$ nm, but its SU appear completely different to that of the zipper structure. The red box highlights the region of the GB from where the SU are displayed in magnified view in Fig. 2 (d). Also here, two characteristic sub-units, marked by green and red circles, are observed. A particular arrangement of four of these sub-units builds up the repetitive unit of the GB. The green sub-unit consists of one "pearl chain" type arrangement (5 atomic columns) and one distorted rectangle (red), similar to the red sub-unit of the zipper structure. The total SU is composed of a combination of these two sub-units, which are mirrored with respect to the grain boundary plane, as is indicated in Fig. 2 (d) by the SU model notation. Here the SU notation is $|\ RP\cdot Я\P\cdot RP\cdot Я\P\ |$, where $R$ represent the distorted rectangle (red), $P$ the pearl chain (green) and the Я and ¶ the mirror operation of the two sub-units with respect to the GB plane. It is obvious that this GB exhibits a longer period structure, since 4 sub-units build up a full SU. Also here, no deviation from this arrangement was observed for the symmetric boundaries. The filled red circles show CSL positions switching periodically from the left to right side of the GB due to the mirror operation of the sub-units. This GB structure is termed pearl structure in the following.

Asymmetric GBs with a small deviation of $\sim 2$–$6^\circ$ from the symmetric orientation are frequently observed for both $\Sigma 19\ b$ boundaries when tracing the GBs. For each GB one example is illustrated in

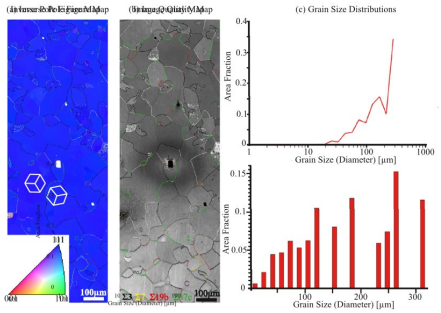


**Fig. 1.** EBSD results of the Cu thin film grown on sapphire: (a) The inverse pole figure map shows a [111] texture of the Cu film. The colored lines indicate the different GBs species in the film. The two white cubes show the orientation of the cubic unit cell, further supporting the [111] orientation with different rotations around [111] (b) The image quality map shows the microstructure of the film and the color coded GB types. The most prominent GBs are low angle GBs (white lines), $\Sigma$ 3 twin boundaries (black lines), $\Sigma$ 7 GB (yellow lines), $\Sigma$ 19*b* GBs (red lines) and $\Sigma$ 37*c* GBs (green lines). (c) These two graphs present two different visualizations of the grain size distribution. (For interpretation of the references to color in this figure legend, the reader is referred to the web version of this article.)

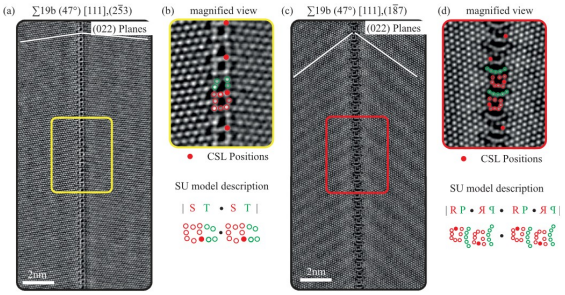


**Fig. 2.** STEM HAADF images of 2 symmetric [111] tilt grain boundaries in plan-view and [111] zone axis orientation. (a) shows the structure of the symmetric $\Sigma$ 19$b$(2$\bar{5}$3) and (c) symmetric $\Sigma$ 19$b$(1$\bar{8}$7) GB. The white lines show the 02$\bar{2}$ planes and the colored boxes indicate the magnified views of each GB structure, depicted in (b) and (d). The green and red dots represent the structural sub-units and the filled dots represent the coincide site lattice positions. On the bottom of (b) and (d), the respective SU model notation is visualized. The meaning of the notation is explained in the text. The STEM images have been smoothed using a Gaussian filter and contrast and brightness were adjusted accordingly. (For interpretation of the references to color in this figure legend, the reader is referred to the web version of this article.)

Fig. 3 (a) and (c). Interestingly, both GBs show a different way of compensating for the asymmetric inclination of the GB habit plane. In case of the zipper structure, the GB dissociates into $\sim$4 nm long symmetric (2$\bar{5}$3) facets that are regularly interrupted by steps as illustrated in Fig. 3 (a) and (b). The magnified view, indicated by the purple rectangle, in Fig. 3 (b) highlights a GB step and shows an extended, disordered core structure. The CSL of the single symmetric facets still fit nicely together (not shown here) so that the step seems to be a shift along the CSL. The facet length, and hence the number of steps, as well as the step height of $\sim$0.5 nm adjusts in such a way as to compensate for the overall deviation in grain boundary plane inclination from the symmetric orientation of $\sim 5^{\circ}$. For the pearl structure, a different scenario is observed, as demonstrated in Fig. 3 (c). Instead of decomposing into facets and steps, here, the asymmetric GB plane remains straight and incorporates additional sub-units to compensate for the asymmetric inclination, as indicated by blue arrows (Fig. 3 (d)). The inset (see Fig. 3 (c)) shows a magnified view of the area highlighted by the blue rectangle. These sub-units appear similar to the "pearl chain" (green sub-unit) of the symmetric case and their repeat distance depends on the magnitude of angular deviation. In the present GB, this deviation is $\sim 3^{\circ}$ and the repeat distance of the extra units is $\sim$2 nm.

### 3.3. Tantalum segregation and grain boundary pinning

Fig. 4 shows conventional and high resolution TEM images of a cross-section specimen of the Cu film alloyed with Ta. The alumina substrate is located at the bottom, the Cu thin film containing a GB in the central region and the 50 nm Ta film is located in the top part of the BF TEM image of Fig. 4 (a). The length of the GB was measured to

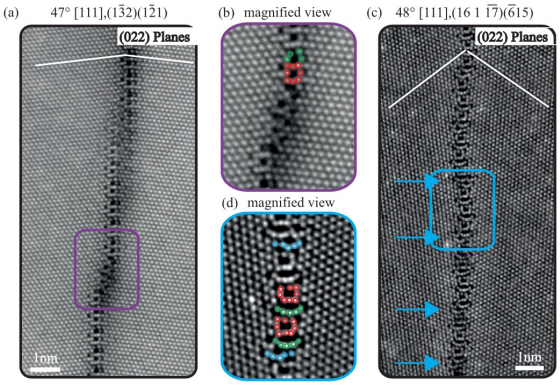


**Fig. 3.** (a) and (c) show asymmetric variants of the GBs shown in Fig. 2 (a) and (c) in plan-view and [111] zone axis orientation. The image depicted in (b), as indicated by a purple box, shows a magnified view of the GB step highlighted in (a). In (d), the magnified view in the blue box shows additional structural sub-units of (c), which are also indicated by the blue arrows. The STEM images have been smoothed using a Gaussian filter and contrast and brightness were adjusted accordingly. (For interpretation of the references to color in this figure legend, the reader is referred to the web version of this article.)

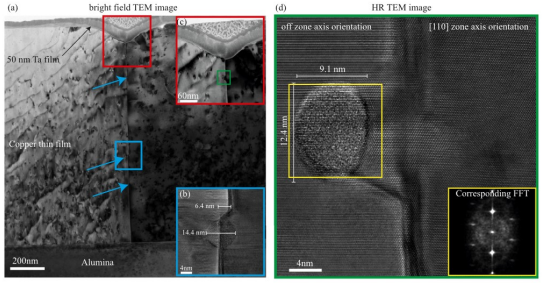


**Fig. 4.** (a) Conventional bright field (BF) TEM image of a cross-section specimen showing the Alumina substrate, the Cu thin film with the GB being perpendicular to the substrate and the Ta thin film. The blue inset (b) shows a spherical particle (HRTEM image) sitting directly on the GB and right in front of a step. The red inset in (c) shows a BF image of another particle sitting next to the GB, which is pinned to the GB. (d) illustrates the atomic structure at that position in a HRTEM micrograph in [011] zone axis orientation. The yellow rectangle includes the particle and shows the position where the FFT was taken from, which is shown in the lower left corner. (For interpretation of the references to color in this figure legend, the reader is referred to the web version of this article.)

$\sim$ 975 nm and its overall appearance is straight. However, the region highlighted by a blue box, reveals a step towards the right grain, as shown in the HRTEM image in Fig. 4 (b). The step size is measured to $\sim$ 6.4 nm. Along the GB three of these steps can be observed, as illustrated by the blue arrows in Fig. 4 (a) so that the total step height between the top and bottom part of the GB adds to $\sim$ 18 nm. Therefore, it can be assumed that the GB migrated towards the right during heat treatment. Furthermore, a spherical Ta precipitate with $\sim$ 14.4 nm in diameter is observed roughly in the middle part of the GB, directly in front of the step (see Fig. 4 (b)). A particle found in the upper GB region (red box) is illustrated in the BF image of Fig. 4 (c). It shows a more elliptical shape with a size of $\sim$ 12.4 x 9.1 nm$^2$ and is directly located besides the GB, while the image contrast reveals that it is still connected to the GB. The high resolution TEM image of Fig. 4 (d) shows that the right grain is in $[011]$ zone axis orientation, while the left grain is off zone axis and only the $(\bar{2}00)$ lattice planes can be resolved. We observe that the grain boundary still adheres to the particle and that the right grain in front of the particle is extended into the region of the left grain, twisting the GB plane. It appears that the GB moved across the precipitate, but was not able to detach from its backside. A STEM-EDS measurement in the same region and magnification as Fig. 4 (d) identifies the particle as a Ta precipitate. An elemental map of the Cu-*Kα* and Ta-*Lα* map is shown in Fig. 5 (a) and the corresponding X-ray spectra, one from the Cu matrix (red) and one from the particle (blue), in Fig. 5 (b). Additionally, a pronounced oxygen peak is observed in the region of the Ta-particle indicating that the particle could be oxidized. However, it should be mentioned that this might also be a result of the FIB sample preparation process and more likely, exposure of the specimen to air during sample handling. From the high resolution image in Fig. 4 (d), the particle appears amorphous. Investigating the fast Fourier transform (FFT) of HRTEM images in other orientations and different particles did also not reveal any indication that the particles are crystalline. An example of an FFT obtained only from the Ta-particle is shown in the inset of Fig. 4 (d).

### 3.4. Zirconium segregation and grain boundary disordering

Adding Zr to the thin film reveals a different segregation behavior than for Ta. The results for an asymmetric $\sim 49^\circ$ $[111]$, $(1\bar{6}5)(1\,\bar{1}\bar{6}\,15)$ GB with the pearl structure is shown in Fig. 6 (a). The planes deviate from the symmetric $(1\bar{8}7)$ plane by $\sim 2.3^\circ$ and $\sim 3.4^\circ$. In the STEM micrograph, the GB appears dark under HAADF conditions and the identification of structural motifs is barely possible. This contrast is observed almost entirely along the GB. A magnified view of the atomic structure is illustrated in the insets of regions highlighted by

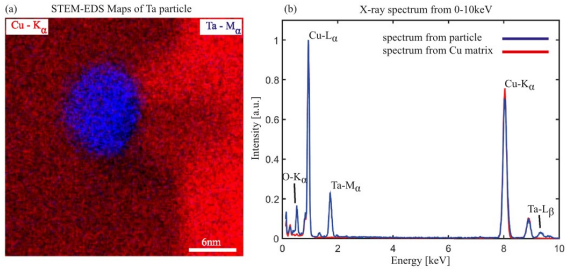


**Fig. 5.** (a) Depicts STEM-EDS maps of the particle using the Cu-$K_\alpha$ (red) and Ta-$M_\alpha$ (blue) edges at the exact position from Fig. 4 d. In (b) two X-ray spectra are plotted together belonging to the pure Cu grain (red) and to the particle (blue). (For interpretation of the references to color in this figure legend, the reader is referred to the web version of this article.)

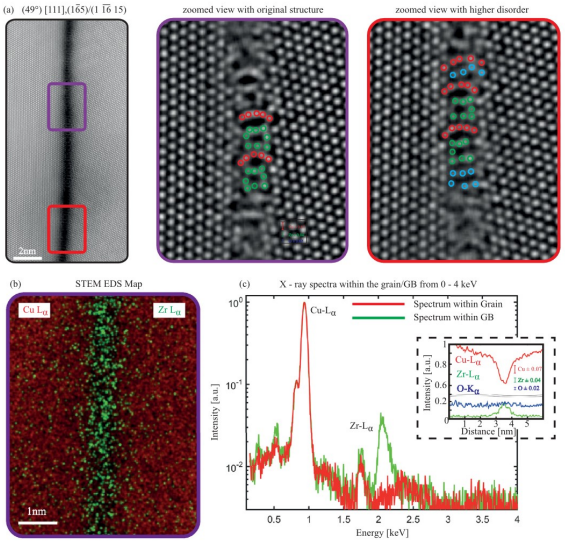


**Fig. 6.** (a) HAADF STEM image in plan-view and [111] zone axis orientation of an asymmetric $\sim 49^\circ$ [111], $(16\bar{5})(1\,\bar{1}6\,15)$ GB alloyed with Zr. The image has been smoothed using a Gaussian filter and contrast and brightness were adjusted accordingly. The insets show two different magnified views of the atomic structure using a strong high pass Fourier filter in order to filter out the dark contrast and to highlight the atomic columns. The purple inset shows a region with the original GB structure and the red region with some deviations, as indicated by the colored dots. (b) STEM-EDS measurements showing maps of Cu-$K_\alpha$ (red) and Zr-$L_\alpha$ (green). The graph in (b) shows the spectra (in log scale of the y-axis) taken from the grain and the GB, showing an increased Zr concentration at the GB. A concentration profile is depicted in the dashed inset of (c), showing the Cu, Zr and O intensity across the GB. The black square block shows the maximum standard deviation of the corresponding element. (For interpretation of the references to color in this figure legend, the reader is referred to the web version of this article.)

purple and red rectangles in Fig. 6 (a). A strong high pass Fourier filter was applied in order to emphasize the structure. Despite the weak atomic column contrast, similar structural units, indicated by green and red dots, as in the pure Cu GB of Fig. 3 (d) can be identified in the purple region. But as shown in the area marked by a red box in Fig. 6 (a), distorted or even disordered variants of the structural motifs are observed. The blue colored atomic columns show additional subunits resulting from the asymmetry of the GB. In the upper region only one line of extra atomic columns is visible, while two extra lines are found in the lower part. The STEM-EDS maps of the Cu-$L_\alpha$ and Zr-$L_\alpha$ X-ray lines taken in the purple region of Fig. 6 (a) are illustrated in Fig. 6 (b) and clearly reveal that the GB is strongly decorated with Zr. The corresponding X-ray spectra, taken from the grain interior (red) and at the GB (green) are shown in Fig. 6 (c). The inset in the spectrum, indicated by a dashed box, illustrates the intensity modulation of Cu, Zr and O by taking a line scan across the GB. The maximum standard deviation of the EDS line profiles was determined by calculating the standard deviation in a sliding window of $\sim 0.5$ nm and is shown as inset in Fig. 6 (c). The peak-to-noise ratio of the integrated Zr-$L_\alpha$ X-ray line profile across the GB is $\sim 4$ indicating clear evidence for Zr enrichment. No clear sign of O enrichment at the GB is observed in the line scan, although a slight oxygen (O) peak is present in the GB spectrum of Fig. 6 (c). All together, Zr leads to a strong disordering of the GB structure, which leads to displacements of atomic column positions perpendicular to the viewing direction. This in turn, leads to de-channeling of the electrons, which leads to an effective reduction of the atomic column intensity in the HAADF images.

In the case of an asymmetric $\sim 49^\circ$ [111], $(12\bar{3})(\bar{2}11)$ GB, adapting the zipper structure, an inhomogeneous segregation of Zr is observed, which appears as dark contrast regions at the GB steps as seen in the HAADF image of Fig. 7 (a) (marked by the white arrows). The corresponding STEM-EDS measurements reveal that these regions are Zr- and O-rich, as can be seen from the corresponding X-ray spectrum extracted from the orange rectangle in Fig. 7 (b). The Zr signal disappears almost entirely at the symmetric GB facets (blue rectangle) and within the Cu matrix (magenta rectangle). This observation is further supported by two intensity profiles extracted across the GB and the GB step, as indicated by arrows. A drop in Cu signal at the GB step is observed, while both Zr and O intensities increase (Fig. 5c). In this line profile the O and Zr signal are more noisy compared to the former example in Fig. 6 (c), again illustrated by the maximum standard deviation shown in the insets in Fig. 7 (c) and (d). In the case of the GB step, the peak-to-noise ratio of the integrated Zr-$L_\alpha$ X-ray line profile is $\sim 2$, which is high enough to confirm segregation of Zr to the GB steps. The O intensity increase may be a result of oxidation of Zr in the GB step, but in view of the APT measurements on a fully Zr decorated GB shown in Fig. 9, a complete Zr-oxide formation is unlikely. The detection of O in each location of the specimen indicates that the surface of the TEM specimen was oxidized. The large Zr rich regions are mainly located at the steps between

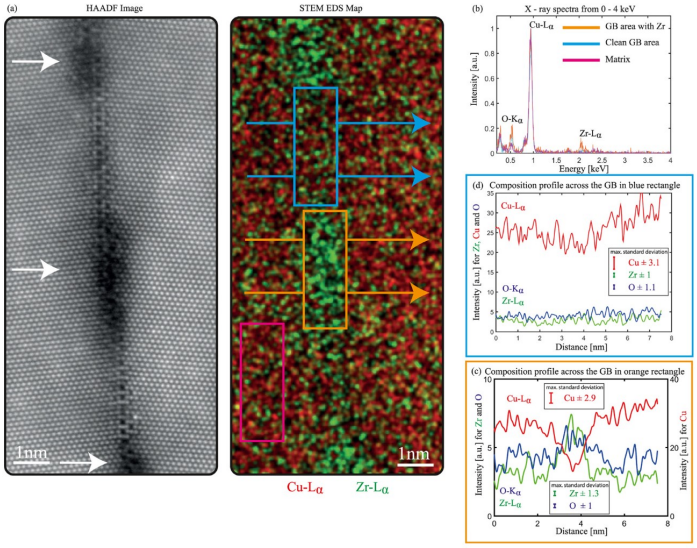


**Fig. 7.** (a) HAADF-STEM micrograph in plan-view and [111] zone axis orientation and STEM-EDS map (Cu-$K_\alpha$ (red) and Zr-$L_\alpha$ (green)) of an asymmetric variant of the zipper structure showing Zr segregation to the GB steps. The colored boxes in the EDS map indicate the positions where the spectra in (b) were taken from. The plot in (b) compares the X-ray spectra from the GB step, the GB between the steps and the grain. The arrows represent the concentration profiles in (c) and (d) and the black square blocks show the maximum standard deviation of the corresponding element of the line scan. The STEM images have been smoothed using a Gaussian filter and contrast and brightness were adjusted accordingly. (For interpretation of the references to color in this figure legend, the reader is referred to the web version of this article.)

symmetric segments, but also smaller Zr-rich regions in the clean symmetric segments are rarely observed (seen also as black contrast), as illustrated in Fig. 8 (a) in the green rectangle. A 0.5 nm wide dark spot can be seen in the middle of the clean symmetric facet, indicating that also here small amounts of Zr could be located in such confined regions. While the facets of the clean GB show a homogeneous length distribution, the facet length in the Zr segregated case varies between 1 nm (first facet in Fig. 8 (a)) and 6 nm (facet in the image center in the green box). This can either be induced by the Zr segregation or could also be due to the local GB curvature. Such a behavior was not observed for a clean GB, but the statistics on these observations is low. Furthermore, the steps differ in contrast with respect to each other, suggesting that the amount of Zr differs for each step.

Since the quantification of STEM-EDS data obtained under strong channeling conditions used here is limited, more precise information on the GB composition was obtained by APT shown in Fig. 9. As EBSD measurements were not successful, because of the remaining Zr film on top of the Cu, it is not known what kind of GB was investigated here. But it still gives very good and detailed information about the elemental distribution and the amount of Zr segregated to the GBs. To directly relate the GB structure and chemistry, one would need to do correlative TEM and APT measurements. The reconstruction in Fig. 9 (a) shows all Cu atoms as red and Zr atoms as green dots. Zr is segregated homogeneously along this GB and its accumulation can be better approximated in the concentration profile (see Fig. 9 (c)). In the corresponding mass spectrum, no significant amount of oxygen was found within the detection limit. It is concluded that pure Zr is located at the GB core and no intermetallic Cu–Zr phases or a $Zr_xO_{1-x}$ were formed, as intended by the annealing treatment. The solute atomic excess of Zr at the GB was calculated following ref [58,59] with an average of $2.76 \pm 0.24\, at \cdot nm^{-2}$. The absence of oxygen signal in the APT data supports that variations in the oxygen signal of the STEM-EDS data are mainly related to surface oxidation.

Looking deeper into the atomic structure of the symmetric, Zr free appearing facets, an influence of Zr on the structural sub-units can be observed. Such regions are marked by a green and orange rectangle (facet and step region) and its magnified views are illustrated as an inset in Fig. 8 (a)). The atomic structure of the Zr decorated steps (orange box) is strongly disordered (compared to the clean step from Fig. 3 (b)), which also explains the decrease in contrast despite the segregation of an atomic species with higher atomic number than Cu. In certain locations, the SU observed at clean symmetric and asymmetric GBs (Figs. 2 (a) and 3 (a)) appear to undergo slight structural transitions upon Zr segregation. Locations of these structural modifications are indicated by yellow rectangles in the insets of Fig. 8 (a). In contrast to the original SUs, the modified units are only composed of rectangular building blocks (red sub-units) leading to a disruption of the periodicity of GB structural units. In Fig. 8 (b), the structure of the clean symmetric and asymmetric GB are compared with the Zr decroated symmetric facet. The blue and yellow boxes show the SU of the clean and Zr segregated GBs. On the bottom of Fig. 8 (b) the structural transition is visualized. The transformation can be described by adding one atomic column to the green, trapezoidal SU, which transforms it into the red, rectangular SU. This seems to occur randomly along the GB facets so that the overall periodicity and order is decreased.